Article type: Original Research Article

Corresponding author info:

Corresponding Author:

Xintian Chi, University of Bristol, Queens Building, University Walk, Bristol, BS8 1TR, England, UK

Email: xintian.chi@bristol.ac.uk

Modal-based vibrothermography using feature extraction with application to composite materials

Xintian Chi[1], Dario Di Maio[2 3], Nicholas A. J. Lieven[1],

1 Department of Aerospace Engineering, University of Bristol, Bristol, England, UK

2 Faculty of Engineering Technology, University of Twente, Enschede, Netherlands

3 Department of Mechanical Engineering, University of Bristol, Bristol, England, UK

Abstract

This research focuses on the development of a damage detection algorithm based on modal testing, vibrothermography and feature extraction. The theoretical development of mathematical models is presented to illustrate the principles supporting the associated algorithms, through which the importance of the three components contributing to this approach is demonstrated. Experimental tests and analytical simulations have been performed in laboratory conditions to show that the proposed damage detection algorithm is able to detect, locate and extract the features generated due to the presence of sub-surface damage in aerospace grade composite materials captured by an infrared camera. Through tests and analyses, the reliability and repeatability of this damage detection algorithm are verified. In the concluding observations of this article, suggestions are proposed for this algorithm's practical applications in an operational environment.

Keywords

Structural health monitoring, damage detection, infrared thermography, vibrothermography, feature extraction, principal component analysis, independent component analysis, modal testing, finite element analysis, composite materials

1. Introduction

With the increasing complexity of modern engineering structures in terms of both the number of components and the process in which the components are assembled, conventional damage detection techniques are often unable to detect the damage effectively. A particular challenge is the more routine use of composite materials in industries, which has brought in new problematic damage mechanisms such as delamination. Effective and efficient non-destructive testing and evaluation (NDT&E) techniques appear to be more necessary than ever with rapid developments in manufacturing engineering.

In the area of NDT&E, ultrasonic C-scan has been the de-facto industry standard because of its high accuracy and strong penetrative capabilities. There has been a substantial volume of research demonstrating the accuracy and reliability of ultrasonic C-scan in damage detection, location and characterization, especially when applied to composite materials.[1 2 3] However, damage detection techniques based on ultrasonic waves are beset with operational challenges that can restrict their practicability and efficiency. In general, the inspected object is required to be physically accessible, water-resistant, homogeneous, with adequate size and smooth surface for accurate inspections with ultrasonic NDT.[4 5]

Infrared thermography (IRT) being another member in the most commonly deployed NDT&E technique category has several unique advantages, which makes IRT able to fill the void left by—or even replace—ultrasonic NDT in some situations. Specifically, it has an operational advantage in being able to scan a large area within short measurement time.[6] The results, which are two-dimensional thermal images or videos, can provide a robust demonstration of the condition of the inspected object so that the analyses of results from IRT inspections are generally simpler and less time-consuming compared to most other NDT&E techniques. These combined advantages make IRT an excellent choice for damage detection of large structures because of its high efficiency from low measurement and data processing time.

Conventional IRT requires thermal radiation as the input, either passively or actively, so that the temperature increase or decrease—depending on local thermal diffusivity—in the damaged region can be detected, with which the damage location can be associated and identified.[6] Vibrothermography is a specific application of IRT utilizing the vibration of the structure, in which the vibration generates friction around the defects. The friction will then cause local temperature to increase through heat generation, which can be captured by an infrared (IR) camera. Due to the friction-based nature of vibrothermography, it is especially effective in detecting cracks and delamination.[7] However, in order to apply vibrothermography correctly, dynamic properties—specifically modal parameters—of the inspected object are required so that the behavior—in particular the distribution of strain—of the object during vibration can be revealed, interpreted and utilized. The acquisition of the modal parameters requires modal testing to be performed, which usually includes the finite element (FE) modal analysis, experimental modal testing and updating of the FE model.

In IRT, the temperature data are acquired from a complex process starting with the electromagnetic radiation of the inspected item, from which the surface temperature can be calculated based on Planck's law and Stefan-Boltzmann law.[8] The results are usually two-dimensional thermal images, each of which contains a table of temperature data. These images always contain multiple features, each generated by an independent heat (or cold) source. These mixed features can be separated with properly selected feature extraction techniques, such as principal component analysis (PCA) and independent component analysis (ICA), so that the results become easier to analyze and interpret.[9 10 11]

In this article, a damage detection algorithm based on modal testing, vibrothermography and feature extraction is presented. Multiple laminated plates made of aerospace grade composite materials were used as the specimens, in which artificial defects were created. However, the damage detection approach presented here is also able to detect most common damage types in a wide context in structures made of other types of materials, given that there is sufficient friction around the damage sites. The analytical justification, experimental procedures, measurement results and analysis outputs of the three components contributing to this damage detection algorithm are demonstrated and explained in this article. A comparison of the results from the vibrothermographic test and result from an ultrasonic C-scan test is included to verify the reliability of the vibrothermography-based damage detection approach. In the concluding observations of this article, the potential improvements and modifications that can be made for this damage detection algorithm to extend into more practical industrial applications, as well as the future work, are also presented and discussed.

2. Literature review

In the area of damage detection through IRT, there has been a substantial volume of research and associated published articles, a subsection of which has a specific focus on vibrothermography and/or feature extraction. Ibarra-Castanedo et al.[12] compared pulsed thermography, lock-in thermography and vibrothermography when applied to aerospace materials, showing that vibrothermography has greater capability in determining deeper damage than the conventional methods because of the internal heat generation which shortens the travel distance of the thermal waves. Renshaw et al.[13] studied the sources of heat generation in vibrothermography with externally applied excitation forces. Using conventional active thermography as the damage detection vehicle, Gao et al.[14] applied three different commonly used feature extraction techniques, namely PCA, ICA and non-negative matrix factorization (NMF) to show that these techniques are able to separate the thermal patterns generated by visible features on the surface of a thin steel plate. Apart from vibrothermography which relies on vibration, there are other similar damage detection principles based on IRT, such as thermoelastic stress analysis that measures the temperature change due to deformations caused by quasi-static or low frequency elastic cyclic stresses.[15 16 17 18]

However, to the authors' knowledge, there has been limited research that combines modal testing, vibrothermography and feature extraction, which are the three

components sequentially demonstrating the capability of determining the damage detection. Compared to past research outcomes focusing mainly on the processing of data from IRT inspections, the main novelty of this research is the inclusion of vibrothermography, which covers the detailed procedures on the execution of vibrothermographic inspections. Vibrothermography has distinct advantages over conventional IRT techniques in detecting cracks and delamination due to its friction-based heat generation mechanism, such as the delamination in the aerospace grade composite plate studied in this research. However, in research activities that involve vibrothermography, the importance of modal parameters and strain distributions has often been overlooked. [19] [20] [21] [22] These omissions almost always result in poor or incorrect choices of excitation frequency and location which are unable to excite the (correct) resonance of the inspected object effectively, so that a high amplitude for the excitation force has to be used to generate sufficient strain to reveal local damage sites.

Excitation forces with unnecessarily high amplitude can initiate additional damage to the structure or exacerbate the existing damage. This phenomenon can be significantly problematic if the specimen is made of laminated composite materials which are intrinsically vulnerable to impacts or high strain rates. [23] [24] [25] [26] [27] [28]

The excitation frequency and/or location chosen without sufficient justification can also harm the reliability and repeatability of the damage detection algorithm significantly. Some regions cannot have a high strain energy with a poorly selected excitation frequency and/or location so that the damage in these regions are unable to be detected due to the lack of friction.

3. Algorithm overview and theoretical background

In the preparation phase of the vibrothermographic damage detection process, the dynamic behavior—particularly the strain distribution—of the inspected object during vibration needs to be studied, which ensures the potentially damaged regions have a relatively high level of dynamic response so that there is adequate friction which can generate sufficient heat for detection by the IR camera. This requirement can be achieved through modal testing which calculates the natural frequencies and mode shapes of the structure. The operating deflection shape (ODS) of the structure during vibration is a linear combination of mode shapes of all the modes excited by the driving force, [29] so obtaining the natural frequencies and mode shapes of the structure is the key to understanding the dynamic behavior of the structure in operating conditions.

3.1. Modal testing

Before the start of the experimental tests, preliminary FE modal analyses should be performed, which estimate the natural frequencies and mode shapes of the relevant modes of the inspected object. These results can provide the guidelines for the selection of the frequency range and location of the applied excitation force in experimental modal testing.

After the preliminary FE modal analyses, the inspected structure should be subject to corresponding experimental modal tests, where its actual modal parameters are measured. For modal testing using electrodynamic shakers, chirp or (pseudo)random signals are usually used to create frequency windows for excitation and measurement.

The measured modal parameters are used to verify the reliability of the preliminary FE model, which usually results in the requirements on the updates of the preliminary FE model in order to reduce the discrepancies between results from the experimental tests and the FE analyses.

3.2. Vibrothermography

The verified—or updated—FE model serves the role of providing high-definition mode shapes and strain energy distribution maps of the relevant modes of the specimen. These outputs from the FE analyses are the crucial references during the selection of excitation location and frequency in the vibrothermographic test section of the damage detection process so that the right resonance—or resonances—can be excited effectively which exhibit a viable strain distribution across structure. The vibration response with the correct modal distribution will increase friction in the damaged region so that the heat generation and temperature rise can be increased as well, which boosts the chance of successful damage detection.

In vibrothermographic testing, the heat generation mechanism due to friction can be explained mathematically. First, the total work done by external forces acting on the structure consists of two parts

$$W = W_{applied} + W_{conservative}, \quad (1)$$

where $W_{applied}$ is the work done by the applied force and $W_{conservative}$ is the work done by the conservative forces such as gravitational force. When there is no energy loss in the system, the total work done by the applied force equals to the changes in the total mechanical energy of the structure, which can be divided into kinetic energy and potential energy

$$W_{applied} = \Delta K + \Delta U. \quad (2)$$

For an elastic body, the potential energy, in this case, is in the form of strain energy, which is the energy stored in an elastic body upon deformation under external forces.[30] The mathematical expression of strain energy can be written as

$$U = \frac{1}{2} F\Delta = \frac{1}{2} V\sigma\varepsilon, \quad (3)$$

where F is force, Δ is displacement, V is volume, σ is stress and ε is strain.

When the vibration of the structure is taken into consideration, the energy in the structure changes between the form of kinetic energy and potential energy, or strain energy in this case.[31] When the structure reaches the maximum deflection in each vibration cycle, there is an instantaneous moment when the structure is (quasi-)stationary, so (almost) all the mechanical energy is in the form of strain energy. Similarly, when the structure is at the equilibrium state, the vibration velocity is at maximum, so all the mechanical energy is in the form of kinetic energy.

In real situations where energy loss is unavoidable, an amount of mechanical energy in the system will be lost in each cycle of vibration. When the major source of energy loss is frictional heat generation, the amount of energy loss due to friction is determined by several parameters, which are the shear stress τ between the contact surfaces, the total length of the relative movement (slip path) γ and the area of contact A, [7] so that the total frictional heat generation on area A is

$$P_A = \iint P_{fr}\, dA = \iint \tau\gamma dA, \quad (4)$$

It is worth noting that there are other relatively minor sources of heat generation, such as plastic heat generation, viscoelastic effect and thermoelastic effect. [7 13]

For frictional heat generation, the shear stress in the contact region can be calculated from contact pressure p and friction coefficient μ, so that

$$\tau = \mu p. \quad (5)$$

As shear stress in the contact region, which accounts for the heat generation, is directly proportional to the contact pressure that is the normal stress in this area, and the magnitude of the elastic deformation in the contact region determines the total length of the slip path in each cycle of vibration, a proportional relationship can be established between the local strain energy and the heat generation due to friction in this area, given that the friction coefficient and the area of contact remain mostly unchanged. This proportional relationship between temperature rise and applied stress (or strain) is also described in the thermoelastic effect. [32]

The ODS of the structure during vibration is a linear combination of the mode shapes of all excited modes of vibration. The proportional relationship between the temperature increase and strain energy due to applied stress should be aligned with the selection of a target mode—or modes—so that the potentially damaged region has high strain energy in an operating condition during vibration and is thus able to cause a relatively large amount of heat generation in the damaged region, which increases the chance of successful detection.

When a single mode of vibration is considered, in order to excite the target mode effectively, a sinusoidal excitation at the corresponding natural frequency is required. In this case, the behavior of the structure in its operating condition is dominated by this vibration mode and so the ODS will be almost identical to the mode shape of this mode of vibration as long as this target mode is adequately separated from the other modes. [29] Due to the proportional relationship between the temperature increase from friction and strain energy, a mode where the potential damage site has relatively high strain energy is preferred. Conversely, if the damaged region is not exercised by dynamic strain then no heat is generated through this process (according to Equation 4) and so the vibrothermographic detection is compromised.

Besides the requirements on the excitation frequency, a correct excitation location must be selected as well based on the results from the modal analysis to increase the frictional heat generation. This can be achieved by exciting the structure at the anti-node in the target mode, which increases the response in the structure during vibration.

In vibrothermographic testing, with properly selected excitation frequency and location, the relative movement in the damaged region will introduce a relatively large amount of friction, which then causes heat generation and temperature rise that can be captured by an IR camera.

3.3. Feature extraction

The temperature data captured by the IR camera can be processed. The original thermal images formed by mixtures of multiple underlying features generated by different physical sources can be analyzed so that the underlying features can be extracted. Analyses of the separated underlying features are significantly more straightforward compared to analyzing the thermal images with mixed features directly, as the mutual influences and superposition effects between the features are eliminated. This type of process in order to separate and extract patterns and features from a set of data containing multiple samples and features can be completed by a variety of feature extraction techniques, among which PCA and ICA are arguably two of the most popular and most suitable methods in this situation. [9 33]

PCA performs the separation and extraction based on the correlation between the extracted features. The extracted features are orthogonal to each other so there is zero mutual information left which guarantees the zero correlation between the features. The features are ordered according to their relative contributions to the original data set, which can be reflected through the eigenvalue that each feature is associated with. Some less-contributing components can be discarded, which achieves dimensionality reduction and data compression. [34] If dimensionality reduction is not performed, the number of extracted components is equal to the number of signals because of the matrix-based calculation algorithm of PCA. There are two common approaches to performing PCA, some claiming that the singular value decomposition (SVD) approach is more robust than the eigen-decomposition approach due to the information loss in the latter. [35 36]

ICA is performed based on the statistical independence between the features. The premise is that if several signals are from different physical sources, they must be statistically independent, and vice versa. [9] Like PCA, there are multiple approaches to performing ICA, which include the gradient-based methods and non-gradient-based methods. The gradient-based approaches usually rely on gradient ascent/descent or other similar methods such as Newton's method for optimization and the natural gradient method. [9 37] The common gradient-based ICA methods include the information-based infomax ICA, the maximum likelihood approach, the normality-based projection pursuit and the complexity-based complexity pursuit. [9 10 37 38 39 40] The major problem of the gradient-based methods is the user-defined parameters, the inappropriate choices of which can lead to failure of convergence so that the correct underlying features cannot be extracted. These problems lead to the need for more reliable methods that do not rely on the gradient. The most popular non-gradient-based ICA method is the FastICA which replaces the gradient ascent with a fixed-point convergence algorithm while either still using the conventional criteria such as information, normality and complexity or switching to other alternative choices of objective functions. [38 41 42] Multiple sources have proved that FastICA is able to achieve more robust outputs compared to PCA and other

ICA methods in most situations in terms of feature extraction. [10] [11] [43] In fact, PCA can also be integrated into FastICA and other traditional ICA techniques for dimensionality reduction before the feature extraction. [42] Similar to PCA, if dimensionality reduction is not included, the number of extracted components is equal to the number of signals regardless of which ICA approach is used. An important consideration when using FastICA, or any other ICA technique, is that, due to their nature of being an ICA method which does not rely on eigenvalues and eigenvectors, it is unable to order the extracted components effectively without additional calculations. [11] [43] However, this problem can be solved by introducing additional calculations, such as using kurtosis to order the extracted components, which will be demonstrated in Section **Error! Reference source not found.**.

Eventually, the signals extracted by PCA or ICA containing the underlying features can be transformed back to images. The features generated by the defects can be visualized more clearly by deploying a properly defined colormap so that the presence and location of the defects can be confirmed and identified. In this research, through the use of a sub-surface defect in composite materials with additional noise factors (reflections), which will be explained in Section 4.4, it has been verified that FastICA is able to outperform PCA significantly.

4. Experimental development and results

4.1. Rig setup for experimental testing

The experimental tests in this damage detection algorithm consisted of two parts. The first part was experimental modal testing which measures the modal parameters that were to be used for the verification of the FE model. The second part was vibrothermographic testing, during which the damage detection was performed. Those two parts could share the same rig setup, with the only difference being the data collection method. A scanning laser Doppler vibrometer (SLDV) was used for the modal tests to collect the kinematic data while an IR camera was used in the vibrothermographic tests to measure the temperature. To describe the procedure, the picture showing the rig for the experimental tests and its corresponding flowchart are shown in Figure 1 and Figure 2 respectively.

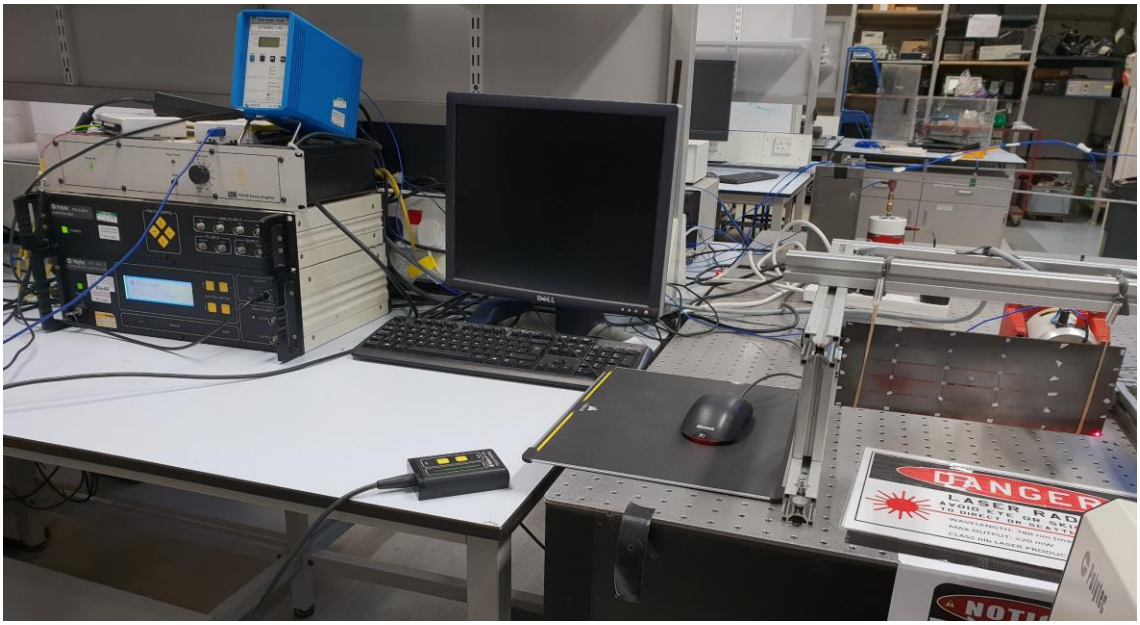

Figure 1: The rig for the experimental tests (with the SLDV for modal testing)

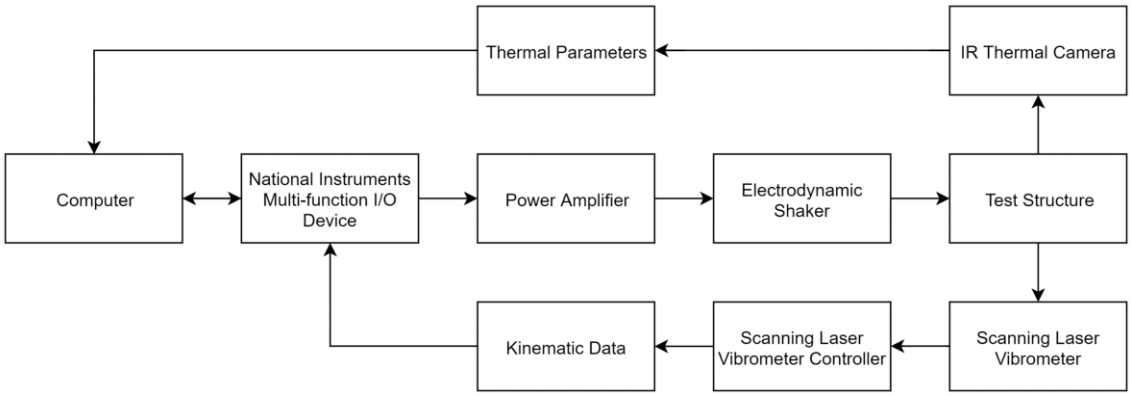

Figure 2: The flowchart showing the procedures of the experimental tests

The specimens used in this research consisted of five originally identical aerospace grade composite plates made of HexPly® 8552 AS4 epoxy matrix woven carbon prepregs composite material which is commonly utilized in primary aerospace structures.[44] The ply angle and stacking sequence was $[45/-45]_{10s}$ except that ply-drops were created on the second and third plies during the manufacturing phase. The dimensions of a complete ply were 260 mm × 100 mm × 0.13 mm. The dropped plies had half the length of a complete ply. The total mass of the composite plate was 96.1 g. Artificial defects were created in the central region of the plates through fatigue, during which the ply-drops were used as a local stress concentrator. Depending on the parameters used in the damage creation, a range of surface features from no to barely visible were left on the composite plates. The central region of the least-damaged and most-damaged specimens are shown in Figure 3.

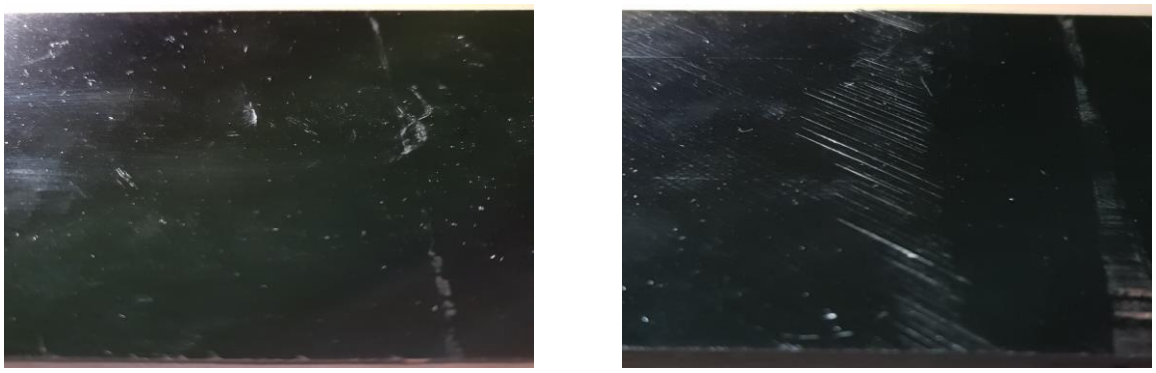

(a) (b)

Figure 3: The (a) least-damaged and (b) most-damaged specimens used in this research project

In both parts of the experimental tests, the specimens were suspended using two springs to avoid unnecessary external forces and constraints, so that the temperature increase at any location other than the excitation point could be guaranteed caused by the vibration of the specimen. The photos showing the specimen suspension and shaker connection are shown in Figure 4.

(a) (b)

Figure 4: (a) The suspended specimen and (b) the attachment point of the electrodynamic shaker

4.2. Preliminary finite element modal analysis

Before the experimental tests, preliminary FE modal analyses were performed using Abaqus 2016 to estimate the natural frequencies and mode shapes of the specimen.

The preliminary FE model was created using the measured dimensions and the material properties provided by Hexcel and other sources. [44] [45] The ply-drops were not included in the FE model as building a perfect FE model was not the main focus of this research. Separately, details on how to create an FE model of a complex engineering

structure and manually update it based on natural frequency difference (NFD) and modal assurance criterion (MAC) can be found in another article from the authors. [46]

The Abaqus built-in composite layup was used deploying a three-dimensional deformable shell to create a simplified model of the composite plate. The model was meshed with S3 elements. After mesh convergence, the seed size was 1 mm globally with a 10% minimum size control to avoid extremely small elements. Free-free boundary condition was used to simulate the suspension in the experimental tests. An FE modal analysis was performed to calculate the natural frequencies and mode shapes of the first ten non-rigid vibration modes of this preliminary model. The first six non-rigid mode shapes and their corresponding strain energy distribution maps superimposed on the mode shapes are shown in Figure 5 and Figure 6 respectively. The natural frequencies of these six modes are summarized in Table 1.

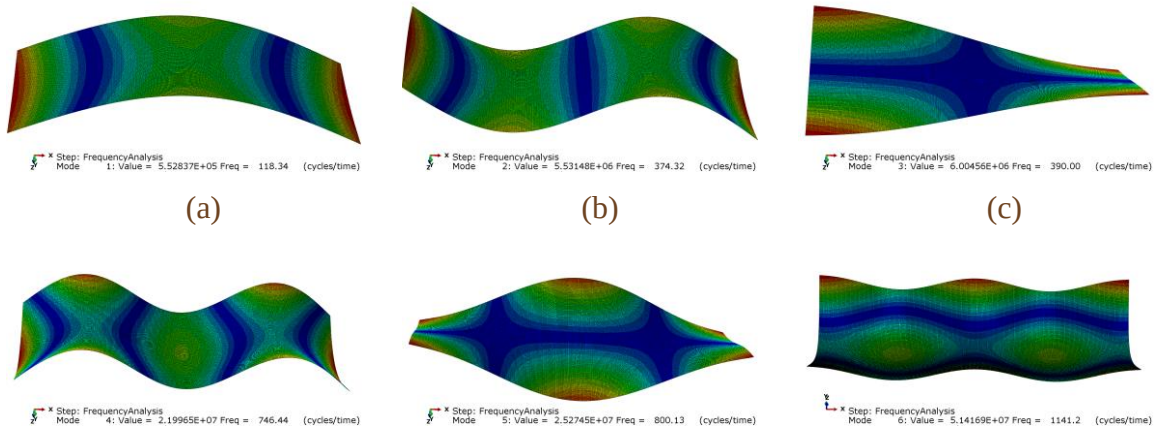

Figure 5: Mode shapes of the (a)-(f) first-sixth non-rigid FE modes

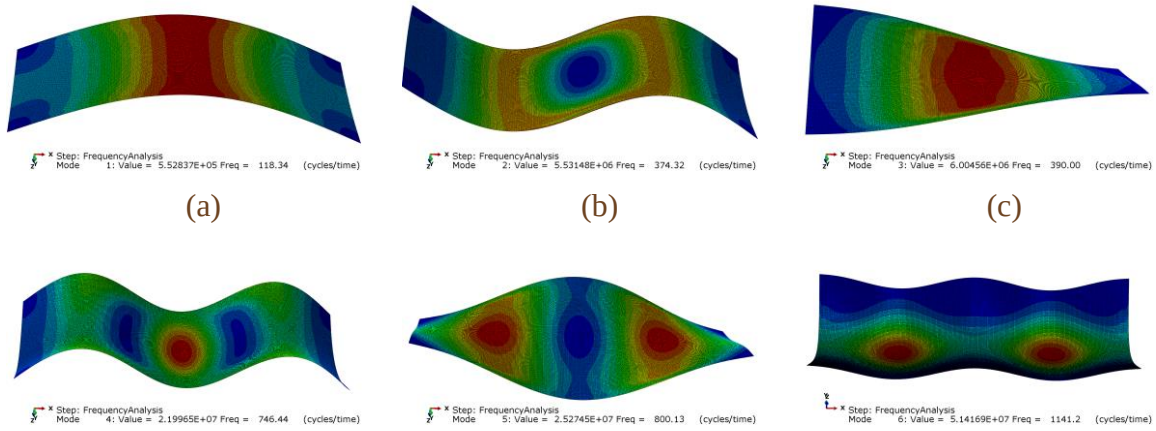

Figure 6: Strain energy distribution maps of the (a)-(f) first-sixth non-rigid FE modes

Table 1: Summary of results from the preliminary FE modal analysis

Mode Number	Natural Frequency	Description
1	118.34 Hz	The first horizontal bending mode
2	374.32 Hz	The second horizontal bending mode
3	390.00 Hz	The first torsional mode
4	746.44 Hz	The third horizontal bending mode
5	800.13 Hz	The second torsional mode
6	1141.2 Hz	The first vertical bending mode

Due to the geometry of the structure, its mode shapes could be easily predicted and explained. However, the natural frequencies measured from the FE modal analysis might be inaccurate because of the omission of the ply-drops in the FE model and the differences in terms of boundary conditions. The exact natural frequencies of the inspected object should be measured through experimental modal tests instead. Apart from the differences in natural frequencies, the ply-drops were also able to cause a local concentration of strain energy that would help the heat generation in that region, which could not be reflected in the FE results.

4.3. Experimental modal testing

The preliminary FE modal analysis was able to provide the options of areas to attach the electrodynamic shaker. By analyzing the mode shapes of the first six non-rigid FE vibration modes, the four corners of the plate were predicted as being the most sensible locations to apply the excitation force, with which all the six modes could be excited effectively. The exact location selected as the excitation point is shown in Figure 4 (b), where an aluminum connector was manufactured and glued onto the composite plate to attach the stinger. An LDS V201 permanent magnet shaker was used to provide the excitation force. Instead of using accelerometer which is the conventional data acquisition tool in modal testing, a Polytec OFV 056 SLDV system was used to avoid the structural mass loading that can cause significant inaccuracies in the results due to the small mass of composite specimen.

During the modal tests, a chirp signal was created for the excitation, which swept from 50 Hz to 1000 Hz over 2 seconds. The selection of this frequency range was also based on the results from the preliminary FE analysis, so that it was expected to cover the first five to ten non-rigid vibration modes, according to the results in Table 1. Ten cycles of measurements were performed, after which the results were averaged using the root mean square (RMS) method to increase the signal-to-noise ratio (SNR) by eliminating the effect of phase noise.[47] A 6×6 grid of points was created on the composite plate for data

acquisition. The exact locations of the 36 points are indicated by the reflective tapes that were required for the SLDV measurement in Figure 7. The measured frequency response functions (FRFs) on the 36 points were used to generate the mode shapes which served the role of verifying the results from the FE modal analysis. Measurement point marked by number 2 was placed at the location of the excitation point on the other side of the plate, whose result is the drive-point FRF shown in Figure 8.

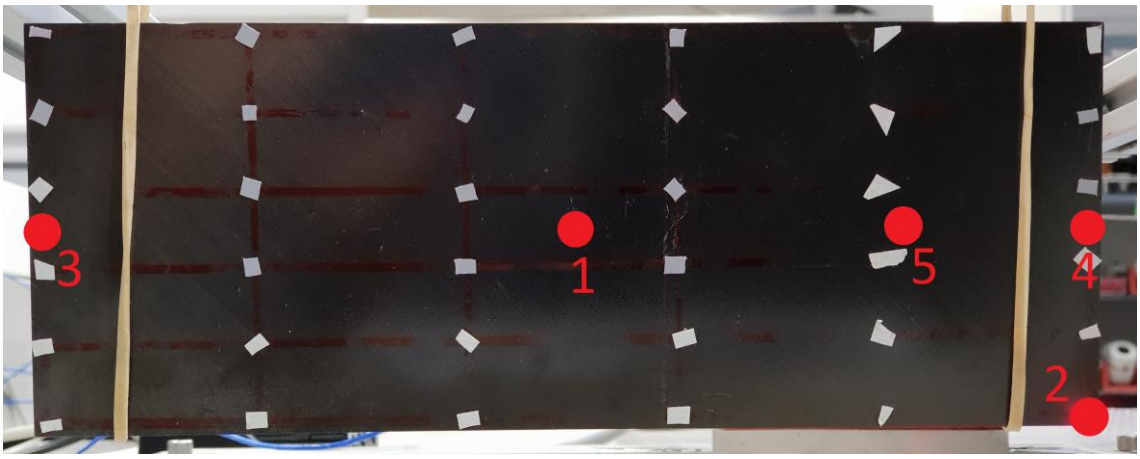

Figure 7: Measurement points located on the plate

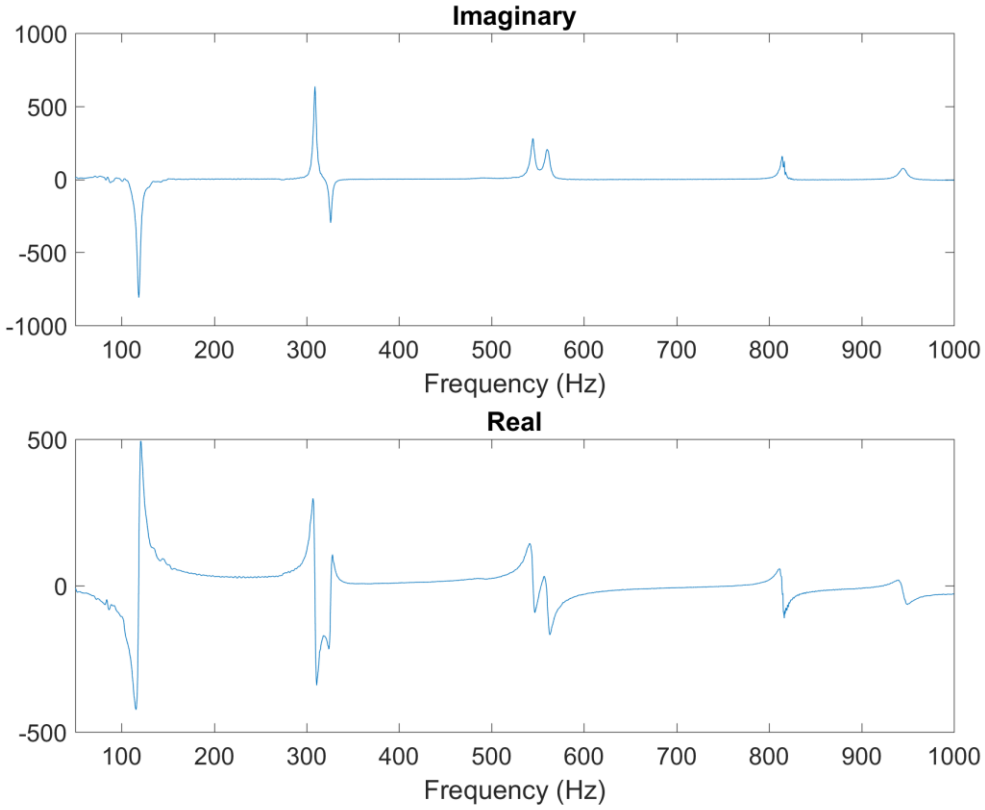

Figure 8: The drive point (point 2) mobility (velocity FRF) plot

As shown in Figure 8, there were seven modes inside the frequency range of the modal test. All experimental modes had lower natural frequencies compared to their FE counterparts. The comparisons are listed in Table 2. Although the inaccuracies in the FE model are able to lead to discrepancies between the experimental and FE results, the major reason is attributed to the altered mass and stiffness matrix caused by the stinger and shaker attachment. As the external conditions would also make a difference in vibrothermographic testing, referring to the experimental results when selecting the excitation frequency for vibrothermographic testing was the more appropriate option.

Table 2: Comparison of natural frequencies from the experimental test and FE analysis

Mode	Natural Frequency (FE)	Natural Frequency (Experiment)	Difference
1	118.34 Hz	118 Hz	-0.28%
2	374.32 Hz	309 Hz	-17.45%
3	390.00 Hz	325 Hz	-16.67%
4	746.44 Hz	543 Hz	-27.25%
5	800.13 Hz	561 Hz	-29.89%
6	1141.2 Hz	814 Hz	-28.67%

Conventionally, the preliminary FE model needs to be updated after experimental modal testing to reduce the discrepancies in natural frequencies (and sometimes mode shapes) between the FE and experimental results. However, as the real natural frequencies of the vibration modes had been measured through the experimental modal test, the sole purpose of the FE model was to estimate the mode shapes and, more important, the strain energy distribution maps of the vibration modes, so that a correct target mode and an appropriate excitation location could be selected for the vibrothermographic tests. Because the preliminary FE model was sufficient in providing this information prior to model updating, FE model updating was not performed.

4.4. Vibrothermographic testing

As discussed in the previous sections, a correct target mode—or target modes— must be selected so that there could be an adequate amount of heat generation in the potentially damaged region when the structure was in an operating condition. The selection of the target mode was based on the strain energy distribution map of each mode, as explained in Section 3.2. The FE model had provided the strain energy distribution maps of the first six non-rigid modes. Among these six modes, the central region where the damage was had relatively high strain energy in the first, third and fourth modes of vibration.

During the creation of the damage, the composite plates were clamped around its vertical center line, as reflected in Figure 3. This left an uncertainty for the exact location

and size of the damage that could be anywhere along the edge of the clamp on the composite plate, which was a consequence of the unknown force distribution during the damage creation. Because of the uncertain location, it was preferable to use a mode of vibration where the whole length of the clamp line had relatively high strain energy. By observing the strain energy distribution maps shown in Figure 6, the first mode of vibration was the most optimal option. In addition, as the first mode of vibration was sufficiently far away from the other modes, exciting the first mode was able to make the ODS almost identical to its corresponding mode shape.

To determine the optimal excitation location, observing the mode shape of the first vibration mode in Figure 5 indicates the middle points of the left and right edges of the plate, which are marked by points 3 and 4 in Figure 7, would be the ideal locations to apply the excitation force. However, because of the resolution and the aspect ratio of the IR camera, covering both the central region and the edge of the plate would reduce the accuracy of the measurement results significantly as the hotspots created at the damage and the excitation point could only contribute to a small portion of the recorded data. Irrelevant features in the background would also be captured. This could add unnecessary challenges to feature extraction, which will be explained in Section 5. Due to these practical considerations, the actual excitation point had been adjusted accordingly so that there were more pixels focusing on the relevant areas. The exact location is marked by point 5 in Figure 7. Other than the changed location of the shaker, the rig setup stayed identical as it was in the modal tests. Another experimental modal test was performed to measure the natural frequency of the first mode with the new excitation location, which gave a result of 119 Hz. The electrodynamic shaker was then set to exert a sinusoidal force at 119 Hz to excite the first mode of vibration.

A FLIR T650sc IR camera, which has a resolution of 640×480 and a thermal sensitivity of 0.02 °C, was used to capture the temperature data. Due to the high reflection capabilities of the surface of the composite plate, barriers were necessary to block the light and minimize the reflections. Two options for the placement of the IR camera when barriers were used are shown in Figure 9.

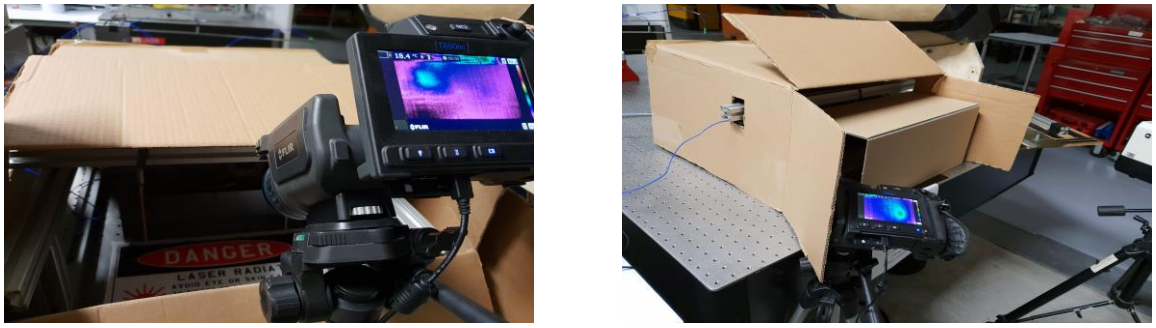

(a) (b)

Figure 9: Two options ((a) and (b)) for camera placements when barriers were used to reduce reflections

It is important to note that the view angle between the camera and the inspected object is able to cause inaccuracies in the measured temperature data, where a larger view angle generally leads to more significant discrepancies between the measured temperature and the actual temperature. This conclusion applies to all real objects. However, for a black body, the emissivity of its surfaces equals to one at any view angle, so that the measured temperature is irrelevant to the view angle.[8 48]

4.4.1. The first vibrothermographic test

The first vibrothermographic test was performed with the camera setup shown in Figure 9 (b). The excitation frequency and location were selected as described previously, where the excitation frequency was 119 Hz while the location is marked by point 5 in Figure 7. A low excitation amplitude (< 10 N) was used to prevent further damage to the composite plate. However, it is important to note that the amount of energy provided by the low-amplitude excitation is limited, in which case the thermal pattern generated by the damage might not be able to reach its maximum potential size due to the outer regions of the damage not having enough heat generation. This observation is confirmed in Section 6, in which the results from the vibrothermographic test are compared with the result from an ultrasonic C-scan test. Among the five specimens created, which are described in Section 4.1, the third least damaged composite plate was used for the vibrothermographic tests.

The data acquisition lasted for 45 minutes, which provided measurement results consisted of 181 frames. The timeline of the events during the first vibrothermographic test is listed in Table 3. The four snapshots mentioned in Table 3 are shown in Figure 10.

Table 3: Timeline of the first vibrothermographic test

Time (min:s)	Event
0:30	The first snapshot (Figure 10 (a)) was taken.
5:00	The electrodynamic shaker was turned on.
5:30	The second snapshot (Figure 10 (b)) was taken.
25:00	The electrodynamic shaker was turned off.
25:15	The third snapshot (Figure 10 (c)) was taken.
45:00	The fourth snapshot (Figure 10 (d)) was taken.

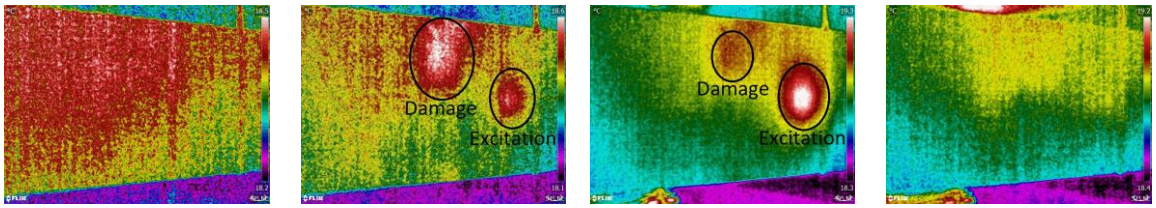

(a) (b) (c) (d)

Figure 10: Snapshots taken at (a) 0:30, (b) 5:30, (c) 25:15 and (d) 45:00 of the first vibrothermographic test

The first picture (Figure 10 (a)) shows the temperature distribution before the start of the excitation, where the maximum temperature difference across the plate was very small (< 0.2 ℃). The second picture (Figure 10 (b)) shows that the hotspots in the damaged region and at the excitation point could be observed clearly after a 30-second excitation, which also demonstrates that the frictional heat generation in the damaged region was stronger than the heat generation due to thermoelastic effect at the excitation point in this situation. In fact, within a very small amount of time (< 4 seconds), the damage was already able to generate a visible hotspot that was captured by the camera, while it took approximately 15 seconds for a visible hotspot to be generated at the excitation point. The third picture (Figure 10 (c)) shows that the heat generated at the damage site already started to show signs of swift dissipation after the shaker had been turned off for 15 seconds, while the hotspot at the excitation point was still clearly visible. The fourth picture (Figure 10 (d)) was taken at 20 minutes after the excitation was stopped, at which moment the heat concentration around the excitation point had finally been fully dissipated. The reason behind the significantly different time for heat dissipation can be first attributed to the different distance from the two heat sources to the surface of the plate. In addition, the heat generated in the shaker was significantly higher than the heat generation in the plate. After the shaker was turned off, the heat transfer between the shaker and the plate continued through the stinger connecting the shaker with the plate.

4.4.2. The second vibrothermographic test

In the previous test, barriers were used to block the light and reduce the reflections. After the completion of multiple additional tests for verification, which had proved the repeatability of this damage detection algorithm, a more practical measurement where there was no barrier used and the IR camera was placed directly in front of the plate was performed. The parameters and boundary conditions remained unchanged from the previous test. The total measurement time was 50 minutes. The timeline of events in this vibrothermographic test is listed in Table 4 and the snapshots mentioned in the table are shown in Figure 11.

Table 4: Timeline of the second vibrothermographic test

Time (min:s)	Event
0:30	The first snapshot (Figure 11 (a)) was taken.
5:00	The electrodynamic shaker was turned on.
6:00	The second snapshot (Figure 11 (b)) was taken.
20:00	The third snapshot (Figure 11 (c)) was taken.
35:00	The fourth snapshot (Figure 11 (d)) was taken.
35:00	The electrodynamic shaker was turned off.
40:00	The fifth snapshot (Figure 11 (e)) was taken.
50:00	The sixth snapshot (Figure 11 (f)) was taken.

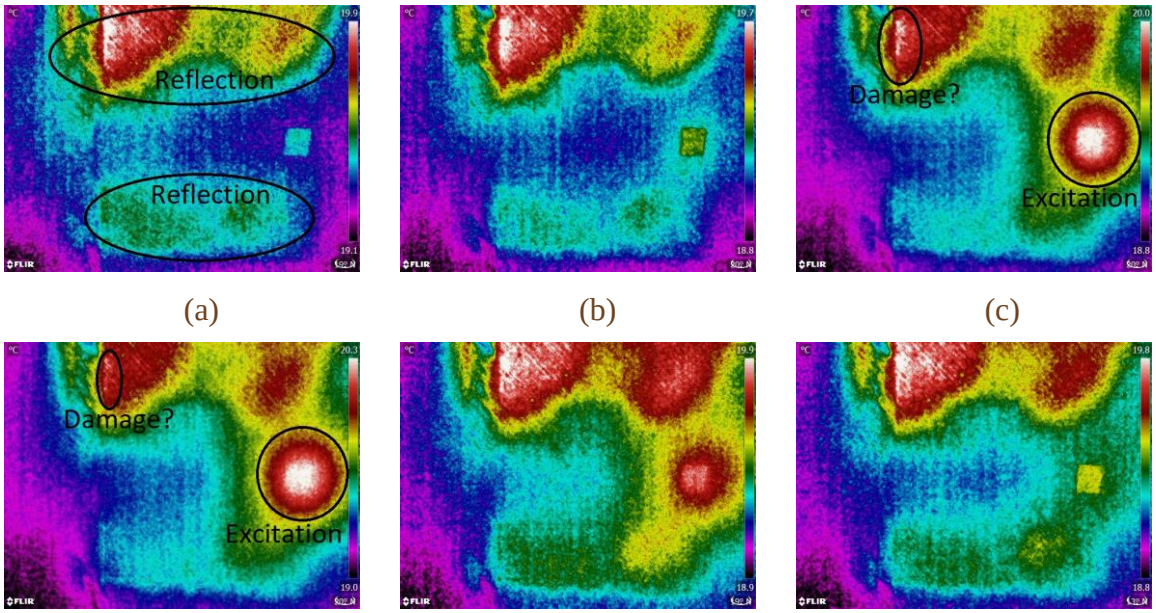

(a) (b) (c)

(d) (e) (f)

Figure 11: Snapshots taken at (a) 0:30, (b) 6:00, (c) 20:00, (d) 35:00, (e) 40:00 and (f) 50:00 of the second vibrothermographic test

The first snapshot (Figure 11 (a)) shows that the reflections of the camera and other irrelevant objects were captured clearly on the composite plate. Based on the experience from the previous tests, the damage should had generated enough heat that could be detected by the IR camera when the second snapshot (Figure 11 (b)) was captured, which was however unable to be found here because it was overshadowed by

the strong reflections. The third picture (Figure 11 (c)) shows that the hotspot at the excitation point could be captured clearly as it was sufficiently away from the reflections. Meanwhile, if close attention is paid, a more localized hotspot can be found in the damage site, which might be a sign of the heat generated by the defect being detected. The fourth picture (Figure 11 (d)) was taken at the moment when the shaker was switched off, which shows the maximum temperature of the plate in this test. The fifth picture (Figure 11 (e)) was taken at five minutes after the excitation was stopped and the temperature distribution in the damaged region became less localized, almost identical to the initial condition, while the hotspot at the excitation point was still clearly visible. The last picture (Figure 11 (f)) shows that the temperature distribution almost recovered to the initial state except that there were still slight traces of undissipated heat around the excitation point even though 15 minutes had passed after the electrodynamic shaker was switched off, which matches the observations from the previous test.

After the completion of the vibrothermographic tests, the recorded results were processed using the two feature extraction techniques, namely PCA and ICA, described in Section 3.3.

5. Data processing with feature extraction

In the results from the two vibrothermographic tests, there were always at least two independent hotspots in the measurement results. Analyzing the raw images with two hotspots might be manageable, but for practical applications where there are tens or potentially hundreds of hotspots in a single image, it is beneficial to isolate and extract these hotspots first so that each independent hotspot and its corresponding physical source can be analyzed without being conflated with influences from other sources.

The eigen-decomposition approach was used for PCA and the FastICA approach was used for ICA. The dimensionality reduction process was not included in either approach. After the extracted components were transformed back to matrices, a 256-color colormap was created based on the jet color scheme in MATLAB, which was then used to visualize the transformed matrices containing the extracted features.

5.1. Feature extraction of the first vibrothermographic test

The data containing 181 frames acquired during the first vibrothermographic test (Section 4.4.1) was processed using both PCA and ICA. Within the two sets of 181 extracted components, only few contained the thermal patterns from the physical sources of interest, such as the hotspots at the excitation point and the damage site.

5.1.1. PCA results

In PCA, the extracted components were ordered automatically according to their contributions to the original data set. The results of the extracted components suggested that the most significantly contributing component was the hotspot at the excitation point, followed by the hotspot of the damage. The first four components from PCA are shown in Figure 12.

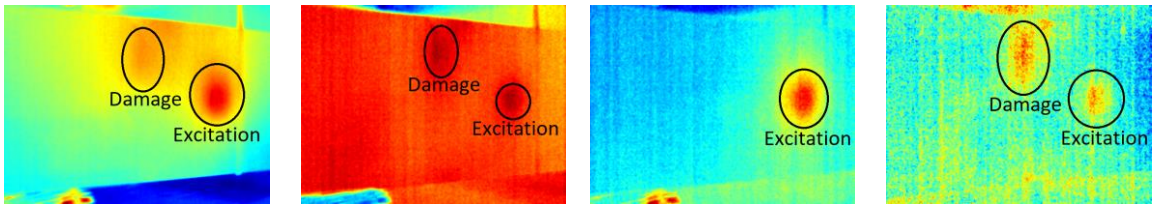

(a) (b) (c) (d)

Figure 12: The (a)-(d) first-fourth components of the first vibrothermographic test extracted using PCA

It is apparent that PCA was not able to completely separate and extract the thermal patterns of the regions of interest. The hotspot generated at the excitation point was extracted and shown in the third principal component (Figure 12 (c)) but the separation of the hotspot generated by the damage was unsatisfactory.

5.1.2. ICA results

During the execution of ICA through FastICA, the additional calculations to order the components were not included so the results were ordered naturally according to the basins of attraction of the maxima with which the extracted components were associated. [41 42] The lack of meaningful order meant that the important components needed to be identified manually. The components that contained the hotspot at the excitation point and the hotspot generated due to the sub-surface defect were not extracted until the 30th iteration and the 44th iteration respectively. This phenomenon shows that additional calculations, such as those based on kurtosis, are necessary to order the components and reduce the difficulties in finding meaningful features.

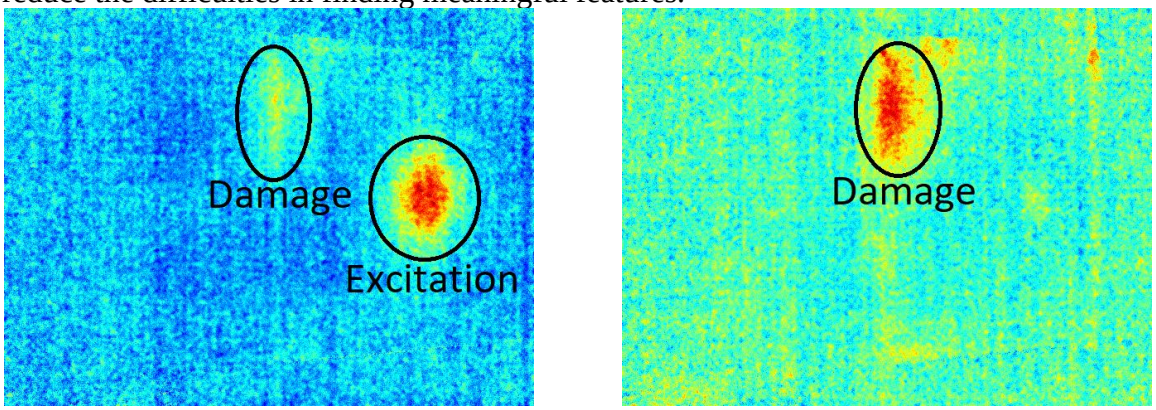

(a) (b)

Figure 13: The (a) 30th and (b) 44th components of the first vibrothermographic test extracted using FastICA

By observing the extracted components in Figure 13, the quality of results was obviously higher than those from PCA, which are shown in Figure 12. This confirmed the conclusions made by previous authors who stated that FastICA, in general, is more robust than PCA in feature extraction, as described in Section 3.3. Although the separation between the two thermal features was not absolute, significant improvements had been shown between the images in Figure 10 and the extracted features in Figure 13.

5.2. Feature extraction of the second vibrothermographic test

The second data set was significantly more challenging because there existed a large number of reflected features and the hotspot of the damage was overshadowed by the strong reflections, as described in Section 4.4.2. The data set contained 200 images, so 200 components were extracted through PCA and ICA respectively.

5.2.1. PCA results

The first three components contained most of the information in the data set despite the additional features due to reflections. These three components are shown in Figure 14.

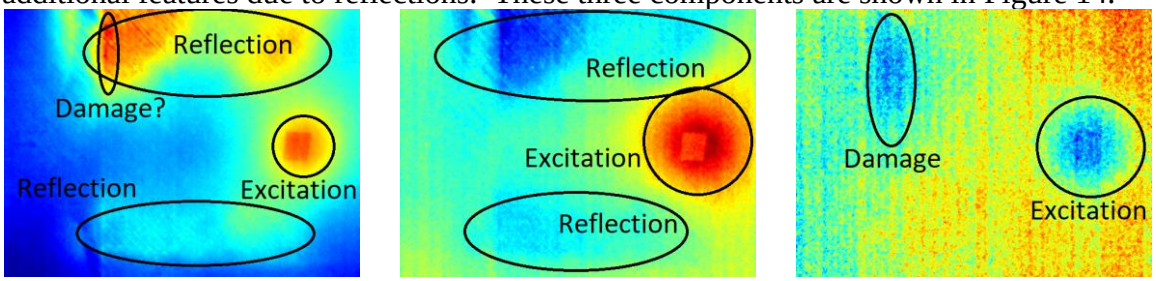

(a) (b) (c)

Figure 14: The (a)-(c) first-third components of the second vibrothermographic test extracted using PCA

The quality of separation results appears degraded compared to those in the previous test because of the increase in the number of features. The first two components were largely dominated by the reflections, and the quality of separation between the reflections and the two hotspots was unsatisfactory. The features from different physical sources were apparently still mixed together, which indicates PCA was unable to achieve the objective of isolating and extracting the two relevant features in this situation.

5.2.2. ICA results

In the 200 components extracted using FastICA, the fourth and 13th components appeared to have captured the two important hotspots respectively while the reflections were contained in the 11th component. These three components are shown in Figure 15.

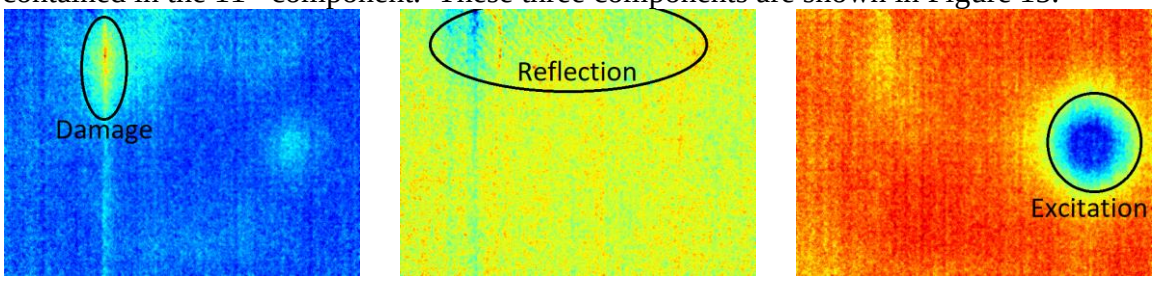

(a) (b) (c)

Figure 15: The (a) fourth, (b) 11th and (c) 13th components of the second vibrothermographic test extracted using FastICA

The two relevant hotspots appear to have been extracted from the mixtures of features successfully despite the strong reflections, although the hotspot generated by the defect was still slightly mixed with other minor features. Compared to the images in Figure 11, the separated features have demonstrated that FastICA is able to improve the quality of the data from IRT inspections significantly, even if a large number of irrelevant features are captured.

From the results processed using PCA and ICA, it is now clear that as the complexity of the data increases where there is a larger number of independent features, the quality difference in results from PCA and FastICA becomes more noticeable.

5.3. Re-ordering of the components extracted by FastICA using kurtosis

Although it has been demonstrated that FastICA is able to outperform PCA, especially when the complexity of the data increases, the lack of meaningful order in the components extracted by FastICA can still pose considerable challenges in an operating condition. In detail, the original order of extracted component is decided naturally by the size of the basins of attraction with which each component is associated with, since optimization methods tend to find maxima with large basins of attraction first. [42] However, the size of the basins of attraction is not directly related to any meaningful physical criterion, so the extracted components are usually in a seemingly random order. This phenomenon is more troublesome if the data are large so that there is a significant number of extracted components. In this case, manual feature selection can be time-consuming.

As briefly mentioned in Section 3.3, kurtosis can be used to re-order the extracted components. Kurtosis is a measure of the shape of a probability distribution. It can be used to measure the difference between a random probability distribution and a Gaussian distribution. The mathematical expression of kurtosis can be described as follows

$$Kurt(x) = \frac{E[(x-\mu)^4]}{(E[(x-\mu)^2])^2} - 3. \quad (6)$$

where μ is the expected value of variable x.

In this case, the kurtosis of any univariate Gaussian distribution is 0. Probability distributions with positive kurtosis are referred to as super-Gaussian. Such distributions are peakier than Gaussian distribution and have fatter tails. Similarly, probability distributions with negative kurtosis are referred to as sub-Gaussian.

Due to the fact that defects are usually small and highly localized, when the thermal images are considered as probability distributions, those containing the thermal patterns of defects are usually extremely super-Gaussian. By re-ordering the extracted components by kurtosis, the meaningful components are likely to appear at more anterior positions, which helps the subsequent feature selection.

With this assumption, the components extracted by FastICA are re-ordered according to their kurtosis values. The comparison between the new orders and the old orders is summarized in Table 5.

Table 5: Comparison between the new orders by kurtosis and the old orders

Test	Component	Old Order	New Order
1	Excitation	30	4
	Damage	44	13
2	Excitation	13	2
	Damage	4	7
	Reflection	11	16

As summarized in Table 5, it is demonstrated that, for the results from the first test, the orders of the meaningful components have shown noticeable improvement. For the second test, the improvement is marginal.

To explain this, as the components are now ordered by their kurtosis values, anterior components usually contain more localized features than the posterior ones. Apart from the meaningful features listed in Table 5, anterior components also consist of irrelevant features in the background, such as those clearly visible in Figure 10, as well as components that contain nothing but image noise.

To conclude, orders from additional calculations such as those based on kurtosis are able to show significant improvement if the original orders determined naturally from the basins of attraction are unable to reveal the true relative significance between the extracted components. However, the new order based on kurtosis is still not perfect, especially that some irrelevant sources are able to generate features more localized than the meaningful ones. In such case, these irrelevant features can appear in a more anterior position due to having a peakier probability distribution. However, the meaningful components are guaranteed to be at relatively anterior positions, while the irrelevant components with more sub-Gaussian distributions are shifted to more posterior positions. This will aid the subsequent feature selection significantly.

6. Verification with ultrasonic C-scan

It has been demonstrated that feature extraction techniques such as PCA and ICA are able to improve the quality of results by separating and extracting the thermal patterns generated by the damage that are captured by the IR camera during the vibrothermographic test. However, the reliability of the original data from the vibrothermographic test is still unverified. As described in Section 1, ultrasonic C-scan is

currently the de-facto industry standard in the area of damage detection, whose result is able to provide the benchmark for alternate techniques. For this reason, an ultrasonic C-scan was performed, during which the central region of the composite plate was scanned. The result is shown in Figure 16.

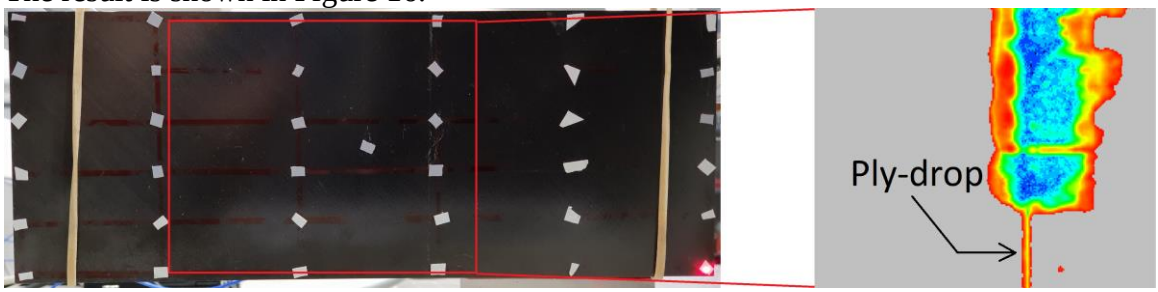

Figure 16: Ultrasonic C-scan result of the central region of the composite plate

By comparing the results from the vibrothermographic tests in Figure 10 and the result from the ultrasonic C-scan in Figure 16, it can be observed that the location and shape of the damage in the vibrothermographic results match those in the ultrasonic C-scan result. Apart from the relatively large sub-surface damage, the ply-drop was also clearly visible in the results from ICA as shown in Figure 13 and Figure 15, despite the fact that it was barely noticeable in the images prior to feature extraction. However, noticeable differences can be found on the size of the damage determined from the vibrothermographic results and the ultrasonic C-scan result. As explained in Section 4.4.1, this discrepancy is mostly attributed to the amplitude of excitation force used in the vibrothermographic tests. Although a relatively low amplitude could protect the specimen from further damage, it was unable to introduce enough relative movement and friction in the damaged region so that the thermal pattern of the damage could not reach its maximum potential size due to the lack of heat generation in the edge areas.

Although differences could still be observed between the vibrothermographic results and the ultrasonic C-scan result in terms of the determination of the size of the damage, the comparison with ultrasonic C-scan confirms that this damage detection algorithm based on modal testing, vibrothermography and feature extraction has been successful in the detection and location of the sub-surface damage. In addition, the measurement time for the vibrothermographic test was considerably shorter than the ultrasonic C-scan, which can be a significant advantage in some practical applications. In detail, as described in Section 4.4, a clearly visible thermal pattern was generated in the damaged region within 4 seconds after the electrodynamic shaker was turned on, while the ultrasonic C-scan usually multiplies this number by several hundred, or even several thousand times, depending on the resolution of the C-scan.

7. Discussion and conclusion

In this research, it has been shown through mathematical analyses in combination with experimental tests that the damage detection approach based on modal testing, vibrothermography and feature extraction is able to detect, locate and extract the thermal features generated due to the presence of sub-surface damage captured by an IR camera.

The theoretical background supporting this damage detection algorithm and the important factors determining the chance of success of the damage detection algorithm have been demonstrated, analyzed and explained in this article.

In modal testing, a representative FE model must be created so that the natural frequencies and mode shapes of the relevant modes of vibration can be calculated which aids the parameter selection in the experimental modal tests. After the completion of the experimental tests, FE updating might be required if the discrepancies between the experimental and FE results cannot be reconciled through usual observation. The results from the modal analyses provide the natural frequencies, mode shapes and strain energy distribution maps of the relevant modes of the structure, from which the parameters used in the vibrothermographic tests can be determined.

In the vibrothermographic tests, if a sinusoidal mechanical excitation force is used, a correct excitation frequency needs to be selected so that the suspected damaged region exhibits relatively high strain energy during vibration. If the target vibration mode excited by the sinusoidal excitation force is sufficiently distant from the other modes, the ODS will be almost identical to the mode shape of the target mode. The target mode can only be excited thoroughly if the excitation force is applied at a region with large displacement in this mode. When the data are being recorded, the location of the IR camera is also a factor that may introduce unnecessary challenges to damage detection because of the reflections and other irrelevant features captured by the IR camera.

In the feature extraction section, it has been demonstrated that both PCA and FastICA are able to improve the quality of data by extracting the underlying features in the original images. It is also verified that FastICA is able to provide more robust results than traditional methods such as PCA, especially when there is a large number of features in the data set. For FastICA, additional calculations, such as those based on kurtosis, can be used to re-order the extracted components. It has been demonstrated that the new orders are able to show noticeable improvement compared to the old orders determined naturally from the basins of attraction, which lowers the challenges in subsequent feature selection.

Apart from the activities completed and outputs produced in this research, improvements and modifications can still be made, especially for the extension of this damage detection approach into the area of more practical industrial applications. The potential improvements and modifications, including future work, are described in the next and final section.

8. Enhancement and future work

In the process of this damage detection algorithm being established, some choices were made to cater for well-rounded tests in a laboratory condition, a part of which, however, conflicts with the practical conditions or is difficult to achieve in real applications so modifications to this algorithm are required to improve its practicality in industrial applications.

In large engineering structures, connections and constraints always exist, some of which can produce additional hotspots due to frictional heat generation or other heat generation mechanisms. The visual access to the inspected object and the locations to place the cameras are usually limited as well so that the existence of reflections and other irrelevant features in the measured data might become unavoidable. All these factors will cause the number of independent features and the influences from the superposition effect to increase, which adds complexity to damage detection. In this case, the data measured when the structure is in different conditions can be used to eliminate some of these irrelevant features, based on the fact that only a portion of the features are independent of the alternating conditions which include operating conditions and environmental parameters such as time, weather, light and temperature.

In this research, a sinusoidal mechanical excitation was used in the laboratory tests because the approximate location of the damage was acknowledged from the outset. However, in more realistic situations, as the objective is to detect and locate the defects, their locations will be unknown. In this situation, a broadband excitation that excites multiple modes should be used, so that there is a high level of strain energy distribution across the entire structure. As explained previously, if there is not sufficient dynamic response in a damage site, the heat generation will be considerably low so that it may be undetectable for the IR camera.

In addition, most real engineering structures are subject to self-induced vibration during their normal mode of operation so that additional excitation is not required. The vibration of the structure usually spans a wide frequency range, so that a large number of modes are excited. In this situation, the ODS of the structure is determined by all self-excited modes of vibration. However, there might still be regions that do not have high strain energy, some of which may actually contain damage and defects, so extra care must be taken in regions with relatively low dynamic response.

Some real engineering structures also have internal heat generations that are irrelevant to vibration. Although they can add complexity to damage detection by introducing additional irrelevant features, these heat generations can also be utilized for damage detection through a traditional passive IRT, and the feature extraction through PCA or ICA can still be performed regardless of the source of the heat as long as there are different time-variant thermal features captured in the measurement results. After the completion of feature extraction, customized colormaps with thresholding can also be used to increase the color contrast in the damage sites to reduce the difficulties in finding the meaningful features.

Another challenge that can be present in industrial applications is the quantity of data because of the scale of the inspected structures. Data compression prior to the execution of feature extraction, as well as dimensionality reduction in conjunction with feature extraction, can be applied to reduce the demand for data analysis and storage.

Apart from PCA and FastICA, other feature extraction techniques may be added for comparison in future works. In addition, the comparison between results from PCA and FastICA was performed directly without quantitative metrics in this research, due to

the fact that the discrepancies are significant. In case that direct inspections are unable to tell the differences directly, which is possible if more feature extraction techniques are used, quantitative criteria for performance evaluation can be utilized for a comparative study.

In addition, although it is demonstrated that additional calculations can be performed to re-order the components extracted by FastICA, which lowers the challenges in the subsequent feature selection, it is possible to reduce the difficulty and increase the efficiency of feature selection even further. A potential solution is the inclusion of machine learning and deep learning, so that neural networks can be designed for automated feature extraction and feature selection. However, due to the specialty of the application, the design of the neural network, and the subsequent training phase, are likely to pose more significant challenges.

Finally but most significantly, the accuracy of the damage detection based on IRT is largely determined by the resolution, sensitivity and location of the camera and the amplitude of the vibration. This implies that damage which produces small and weak hotspots might not be able to be detected due to the spatial resolution of the IR camera compared to the size of the defects and the distance from the IR camera to the inspected object. Correct decision theory needs to be established to estimate the safety condition of the structure even if there is no damage detected. For relatively larger damage, even when the damage is detected successfully, the size determined from the results of vibrothermographic tests might be inaccurate if the damaged region is not excited thoroughly due to the low amplitude of vibration. Further studies on the quantification and characterization of the damage based on results from vibrothermographic tests are still required.

Declaration of conflicting interests

The author(s) declared no potential conflicts of interest with respect to the research, authorship, and/or publication of this article.

Funding

The author(s) received no financial support for the research, authorship, and/or publication of this article.

Research data accessibility

The data produced during this research project and used in this article has been uploaded to Google Drive. The files can be accessed at https://drive.google.com/drive/folders/1PEgyDiz14IWEaRy6lG6eB_UI0qkvaSET?usp=sharing.

References

1. Ruzek R, Lohonka R and Jironc J. Ultrasonic C-Scan and shearography NDI techniques evaluation of impact defects identification. *NDT & E International*. 2006; 39(2): p. 132-142.

2. Gordon GA, Canumalla S and Tittmann BR. Ultrasonic C-scan imaging for material characterization. *Ultrasonics*. 1993; 31(5): p. 373-380.

3. Hasiotis T, Badogiannis E and Tsouvalis NG. Application of Ultrasonic C-Scan Techniques for Tracing Defects in Laminated Composite Materials. In *4th International Conference on NDT*; 2007; Chania.

4. Schmerr LW Jr. *Fundamentals of Ultrasonic Nondestructive Evaluation*: Springer; 2016.

5. Krautkrämer J and Krautkrämer H. *Ultrasonic Testing of Materials*: Springer Science & Business Media; 2013.

6. Meola C, Boccardi S and Carlomagno GM. *Infrared Thermography in the Evaluation of Aerospace Composite Materials: Infrared Thermography to Composites*: Woodhead Publishing; 2016.

7. Stepinski T, Uhl T and Staszewski W. *Advanced Structural Damage Detection: From Theory to Engineering Applications*: Wiley; 2013.

8. Speakman JR and Ward S. Infrared thermography: principles and applications. *Zoology: analysis of complex systems*. 1998; 101: p. 224-232.

9. Stone JV. *Independent Component Analysis: A Tutorial Introduction*: MIT Press; 2004.

10. Hyvarinen A, Karhunen J and Oja E. *Independent Component Analysis*: John Wiley & Sons; 2001.

11. Hyvarinen A. Survey on independent component analysis. *Neural Computing Surveys*. 1999; 2.

12. Ibarra-Castanedo C, Genest M, Guibert S, et al. Inspection of aerospace materials by pulsed thermography, lock-in thermography and vibrothermography: A comparative study. In *SPIE Proceedings Vol. 6541*; 2007.

13. Renshaw J, Chen JC, Holland SD, et al. The Sources of Heat Generation in Vibrothermography. *NDT&E International*. 2011; 44: p. 736-739.

14. Gao B, Bai L, Woo WL, et al. Thermography pattern analysis and separation. *Applied Physics Letters*. 2014; 104(25).

15. Dulieu-Barton JM. Introduction to thermoelastic stress analysis. *Strain: An International Journal for Experimental Mechanics*. 1999; 35(2): p. 35-39.

16. Hack E, Fruehmann RK, Roos R, et al. Flaw and damage assessment in torsionally loaded CFRP cylinders using experimental and numerical methods. *Composite Structures*. 2015; 132: p. 109-121.

17. Tighe RC, Dulieu-Barton JM and Quinn S. Identification of kissing defects in adhesive bonds using infrared thermography. *International Journal of Adhesives and Adhesion*. 2016; 64: p.

168-178.

18. Tighe RC, Howell GP, Tyler JP, et al. Stress based non-destructive evaluation using thermographic approaches: from laboratory trials to on-site assessment. *NDT&E International*. 2016.

19. Li M, Holland SD and Meeker WQ. Statistical Methods for Automatic Crack Detection Based on Vibrothermography Sequence-of-Images Data. *Statistics Preprints*. 2010; 69.

20. Szwedo M, Pieczonka L and Uhl T. Application of Vibrothermography in Nondestructive Testing of Structures. In *6th European Workshop on Structural Health Monitoring*; 2012.

21. Li Y, Yang Z, Luo W, et al. The Use of Vibrothermography for Detecting and Sizing Low Energy Impact Damage of CFRP Laminate. *Advanced Composites Letters*. 2017; 26(5): p. 162-167.

22. He Y, Chen S, Zhou D, et al. Shared Excitation Based Nonlinear Ultrasound and Vibrothermography Testing for CFRP Barely Visible Impact Damage Inspection. *IEEE Transactions on Industrial Informatics*. 2018; 14(12): p. 5575 - 5584.

23. Wang C and Yew CH. Impact Damage in Composite Laminates. *Computers & Structures*. 1990; 37(6): p. 967-982.

24. Bull DJ, Spearing SM, Sinclair I, et al. Three-dimensional assessment of low velocity impact damage in particle toughened composite laminates using micro-focus X-ray computed tomography and synchrotron radiation laminography. *Composites Part A: Applied Science and Manufacturing*. 2013; 52: p. 62-69.

25. Yang FJ and Cantwell WJ. Impact damage initiation in composite materials. *Composites Science and Technology*. 2010; 70: p. 336-342.

26. Richardson MOW and Wisheart MJ. Review of low-velocity impact properties of composite materials. *Composites Part A: Applied Science and Manufacturing*. 1996; 27(12): p. 1123-1131.

27. Tai NH, Yip MC and Lin JL. Effects of low-energy impact on the fatigue behavior of carbon/epoxy composites. *Composites Science and Technology*. 1998; 58(1): p. 1-8.

28. Sjoblom P, Hartness JT and Cordell TM. On Low-Velocity Impact Testing of Composite Materials. *Journal of Composite Materials*. 1988; 22(1): p. 30-52.

29. Ewins DJ. *Modal Testing: Theory and Practice*: Wiley-Blackwell; 1984.

30. Kelly PA. 8.1. Energy in Deforming Materials. In *Solid Mechanics Part I: An Introduction to Solid Mechanics*. Auckland: The University of Auckland; 2015; p. 231-241.

31. Piersol AG. Chapter 7: Vibration of Systems Having Distributed Mass and Elasticity. In *Harris' Shock and Vibration Handbook, Sixth Edition.*: McGraw-Hill Education; 2010; p. 7.1-7.50.

32. Harwood N and Cummings WM. *Thermoelastic Stress Analysis*: CRC Press; 1991.

33. Bishop CM. *Pattern Recognition and Machine Learning*. Cambridge: Springer; 2006.

34. Shlens J. A tutorial on principal component analysis. *International Journal of Remote Sensing*. 2014; 51(2).

35. Sellentin E and Heavens AF. Quantifying lost information due to covariance matrix estimation in parameter inference. *Monthly Notices of the Royal Astronomical Society*. 2017; 464(4): p. 4658-4665.

36. Geiger BC and Kubin G. Relative Information Loss in the PCA. In *IEEE Information Theory Workshop*; 2012.

37. Bell AJ and Sejnowski TJ. An information-maximisation approach to blind separation. *Neural Computation*. 1995; 7: p. 1129–1159.

38. Hyvarinen A. The fixed-point algorithm and maximum likelihood estimation for independent component analysis. *Neural Processing Letters*. 1999; 10.

39. Hyvarinen A. Complexity pursuit: Separating interesting components from time series. *Neural Computation*. 2001; 13: p. 883–898.

40. Stone JV. Blind source separation using temporal predictability. *Neural Computation*. 2001; 13: p. 1559–1574.

41. Hyvarinen A and Oja E. A fast fixed-point algorithm for independent component analysis. *Neural Computation*. 1997; 9.

42. Hyvarinen A. Fast and robust fixed-point algorithms for independent component analysis. *IEEE Transactions on Neural Networks*. 1999; 10.

43. Hyvarinen A and Oja E. Independent component analysis: Algorithms and applications. *Neural Networks*. 2000; 13.

44. Hexcel. HexPly® 8552 Epoxy Matrix Product Data Sheet. 2016.

45. Marlett K. Hexcel 8552 AS4 Unidirectional Prepreg at 190 gsm & 35% RC Qualification Material Property Data Report. 2011.

46. Chi X, Di Maio D and Lieven NAJ. Dynamic response and energy loss in jointed structures using finite element methods: application to an aero-engine casing assembly. In *Proceedings of International Conference on Noise and Vibration Engineering*; 2018; Leuven.

47. NI Spectral Measurements Toolkit - LabVIEW Help. 2014.

48. Nicodemus FE. Directional reflectance and emissivity of an opaque surface. *Applied Optics. 1965*; 4: p. 767-775.